A novel synergy of Er^{3+}/Fe^{3+} co-doped porous Bi_5O_7I microspheres with enhanced photocatalytic activity under visible-light irradiation

Yongbao Liu [a], Gangqiang Zhu [a,b,*], Jianzhi Gao [a,**], Runliang Zhu [b,**], Mirabbos Hojamberdiev [a,c], Chenghui Wang [a], Xiumei Wei [a], Peng Liu [a]

[a] School of Physics and Information Technology, Shaanxi Normal University, Xi'an 710062, China
[b] Guangdong Provincial Key Laboratory of Mineral Physics and Material Research & Development, Guangzhou Institute of Geochemistry, Chinese Academy of Sciences, Guangzhou 510640, China
[c] Department of Natural and Mathematic Sciences, Turin Polytechnic University in Tashkent, Kichik Halqa Yo'li 17, Tashkent 100095, Uzbekistan

ABSTRACT

Uniform porous Bi_5O_7I (BOI) microspheres photocatalysts co-doped with Fe^{3+} and Er^{3+} were synthesized by a solvothermal-thermal decomposition method, in which Er^{3+} with upconversion properties could transform infrared light beyond the absorption edge of Bi_5O_7I into visible light, and also activate the Fe^{3+}-doped Bi_5O_7I (Fe-BOI). The photocatalytic activities of the photocatalysts were evaluated by the degradation of three typical colorless model pollutants, i.e., phenol, bisphenol A (BPA), and chloramphenicol (CAP), under visible light irradiation (800 nm > λ > 400 nm). The results showed that the photocatalytic activity of Fe^{3+}/Er^{3+} co-doped Bi_5O_7I (Er/Fe-BOI) was much higher than that of the undoped, Fe^{3+}-doped and Er^{3+}-doped Bi_5O_7I photocatalysts. In addition, Fe^{3+}/Er^{3+} co-doped Bi_5O_7I exhibited photocatalytic activity under a 3W LED lamp (red light, λ = 630 nm) with the wavelength beyond the absorption edge of Bi_5O_7I, which further testified that the upconversion effect of Er^{3+} generates the enhanced photocatalytic activity of Bi_5O_7I. Photodegradation mechanism was systematically studied by using various radical quenchers and it was revealed that photogenerated holes (h^+) and superoxide radicals ($O_2^{\bullet-}$) actively participated, whereas hydroxyl (•OH) radicals had negligible contribution in photodegradation of phenol.

© 2016 Elsevier B.V. All rights reserved.

1. Introduction

Photocatalysis has attracted extensive attention due to its potential applications in environmental purification and energy saving, which can transform solar energy into clean hydrogen energy through splitting water, and degrade harmful organic substances [1,2]. A variety of photocatalysis have been introduced for the purpose of efficiently purifying the organic-containing wastewater, which has been considered as a cost-effective method [3–5]. Many large band gap (E_g > 3.0 eV) oxide semiconductors photocatalysts, such as TiO_2 [6], ZnO [7], and SnO_2 [8], etc., have been intensively investigated in the field. However, it can only be activated under UV irradiation (λ < 388 nm), and accounts for less than 5% of solar light energ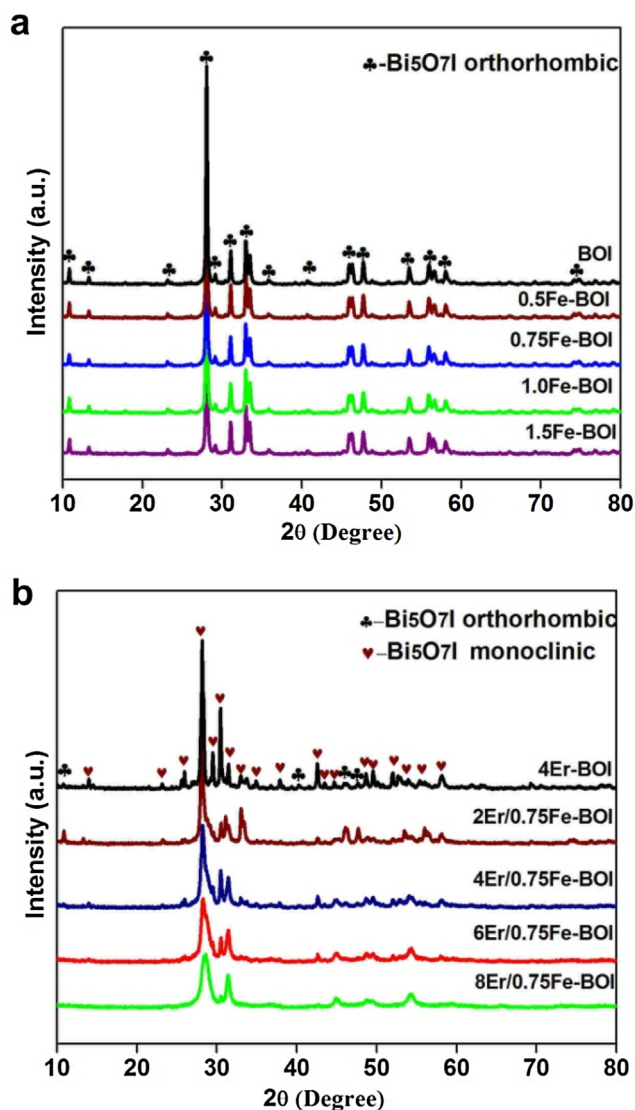y [9,10]. From the viewpoint of solar energy, the development of efficient using solar energy photocatalysts for the photodegradation of organic pollutants has been focused as an urgent issue.

During the past decades, doping with transition metal ions has been widely applied in synthesizing semiconductor photocatalytic material, which can enhance the photocatalytic activity and visible light response [9–11]. First, doping transition metal ions will induce a batho-chromic shift, i.e., a decreasing of the band gap or introduction of intra-band gap states, which could results in more efficient visible light absorption [12]. Second, doping with variable valency metal ions (Cr^{3+}, Cu^{2+}, Mn^{3+}, Fe^{3+}, etc.) in semiconductors can reduce the recombination rate of photo-generated electronshole, hence, generating higher photocatalytic activity [13–15]. In practice, Fe^{3+} ions can form a doped energy-band to reduce the band gap of the photocatalysts, therefore, electrons can be excited by photons at the lower energy level [16]. More importantly, Fe^{3+} can transform into Fe^{2+} and Fe^{4+} ions by trapping photo-generated electrons and holes, respectively, which can reduce the recombination process and enhance the photocatalytic activity [17]. In addition, the radius of Fe^{3+} (0.78 Å) is smaller than that of Bi^{3+} (1.17 Å), so Fe^{3+} ions can be easily doped into crystal lattice of the bismuth-

Fig. 1. (a) XRD patterns of pure BOI, 0.5Fe-BOI, 0.75Fe-BOI, 1.0Fe-BOI, and 1.5Fe-BOI samples; (b) XRD patterns of 4Er-BOI, 2Er/0.75Fe-BOI, 4Er/0.75Fe-BOI, 6Er/0.75Fe-BOI, and 8Er/0.75Fe-BOI samples.

In this work, we first report the fabrication of porous Er^{3+}/Fe^{3+} co-doped Bi_5O_7I sphere through a thermal decomposition of Er^{3+}/Fe^{3+} co-doped BiOI microspheres precursor. The photocatalytic activities of the as-synthesized samples were evaluated by the photo-degradation of phenol, bisphenol A, and chloramphenicol under visible-light irradiation. Furthermore, the possible mechanism for the enhanced photo-degradation was also discussed in detail.
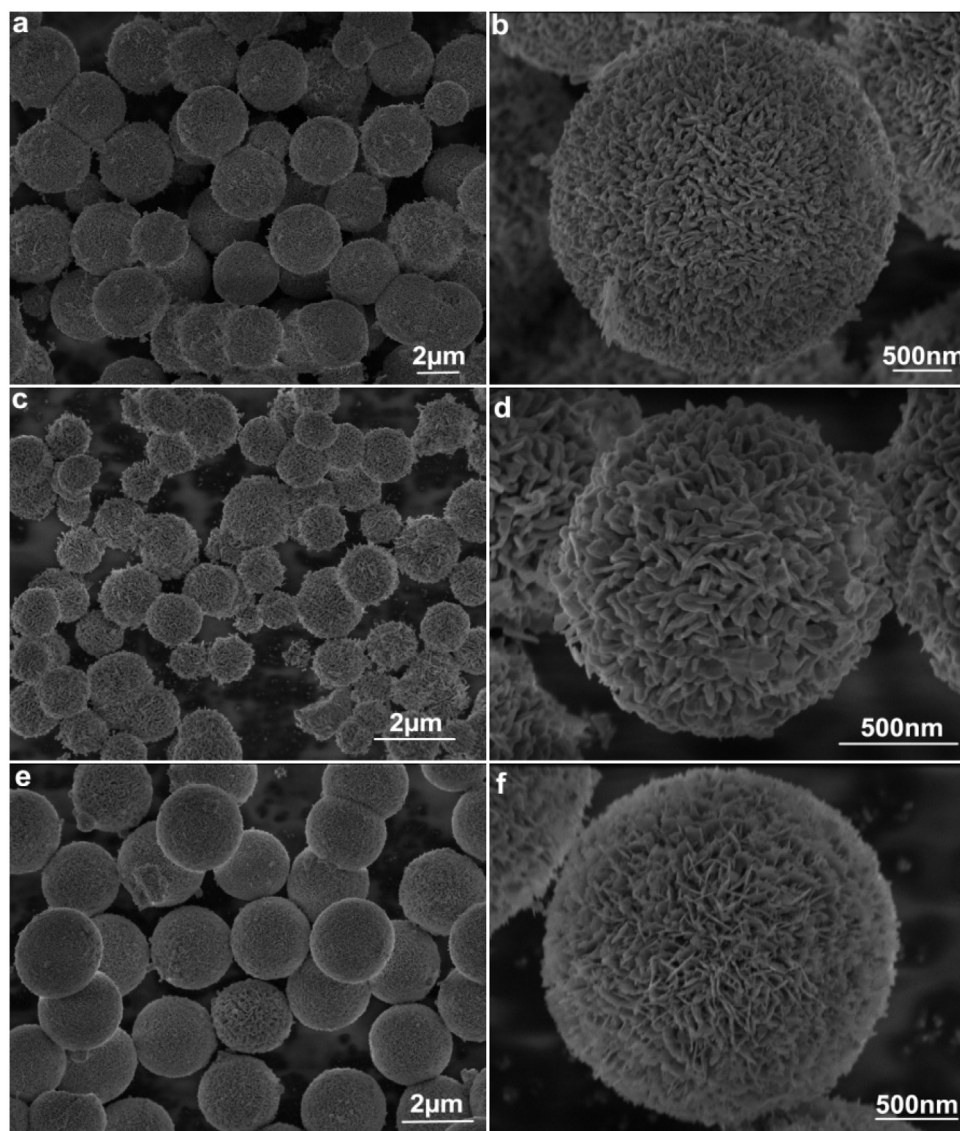
2. Experimental

2.1. Sample preparation

All the chemical reagents were of analytical grade and used without further purification. The Bi_5O_7I samples were first prepared by the ethylene glycol-assisted solvothermal and then calcinations at 450 °C [33]. In a typical synthesis procedure for Bi_5O_7I: Firstly, 1.3825 g of $Bi(NO_3)_3 \cdot 5H_2O$ and 0.5010 g of KI were separately dissolved in 25 mL of ethylene glycol under ultrasonication for 15 min. Secondly, the two solutions were mixed under vigorous stirring for 50 min, and then transferred into a Teflon-lined stainless steel autoclave for reaction at 160 °C for 12 h. The resulting precipitates were washed with deionized water and ethanol for several times, and dried at 75 °C for 12 h. Finally, the obtained precipitates were heated at 450 °C for 2 h in air. An identical experimental procedure was also applied for the synthesis of Fe^{3+}-doped Bi_5O_7I and Er^{3+}-Bi_5O_7I porous microspheres with the addition of 0.5–1.5 at% $Fe(NO_3)_3 \cdot 9H_2O$ or 4at% $Er(NO_3)_3 \cdot 6H_2O$ in the reaction solution, and the as-prepared samples were denoted as 0.5Fe-BOI, 0.75Fe-BOI, 1.0Fe-BOI, 1.5Fe-BOI, and 4Er-BOI, respectively. The synthesis of Er^{3+}/Fe^{3+} co-doped Bi_5O_7I porous microspheres was also performed with the same processes as Fe^{3+}-doped Bi_5O_7I, with the addition of 2–8 at% $Er(NO_3)_3 \cdot 6H_2O$ into the reaction solution, and the synthesized samples were denoted as 2Er/0.75Fe-BOI, 4Er/0.75Fe-BOI, 6Er/0.75Fe-BOI, and 8Er/0.75Fe-BOI, respectively.

2.2. Characterization

The crystalline phases were determined by X-ray powder diffraction (XRD) at room temperature with Cu Kα radiation on a Bruker D8 Advance instrument in 2θ range of 10–80°. The scanning electron microscopy (SEM) images were recorded by a field emission scanning electron microscopy (Nova NanoSEM 450, FEI). The transmission electron microscopic (TEM) images of the samples were carried out by using a JEM-2100 electron microscope (JEOL, Japan). The chemical states of elements in the samples were determined by X-ray photoelectron spectroscopy (XPS) using a VG ESCALAB MKII X-ray photoelectron spectrometer (VG Scienta, USA) with Mg Ka radiation. The Brunauer–Emmett–Teller (BET)-specific surface areas and porosity of the samples were measured by a N_2 gas adsorption method using an ASAP 2020 instrument (Micromeritics). The samples were degassed at 120 °C for 5 h prior to N_2 gas adsorption measurements. The S_{BET} values were obtained by a multipoint BET method using the adsorption data in the relative pressure (P/P_0) range of 0.05–0.3. The pore size distribution was calculated by the Barrett, Joyner, and Halenda (BJH) method using the desorption isotherm. Inductively coupled plasma mass spectrometry (ICP-MS, AURORA M90, Bruker) was employed to analyse the bulk elemental composition of the samples. The UV–vis adsorption spectra of the samples were measured on a Cary 5000 (Agilent, USA) UV–vis-NIR spectrophotometer. The electronspin resonance (ESR) signals of radicals spin-trapped by spin-trapreagent DMPO (Sigma Chemical Co.) were examined on a ESR spectrometer (JES-FA200, Bruker).

based semiconductor photocatalysts [18]. Indeed, many studies have focused on doping of Fe^{3+} into the bismuth-based semiconductors photocatalysts, such as $BiVO_4$ [19], BiOCl [20], Bi_2O_3 [21], Bi_2WO_6 [22], etc., resulting in the enhanced photocatalytic activity compared to the un-doped counterpart.

In recent years, many researchers have devoted their works to enhancing the photocatalytic activity at near infrared light, and doping with rare earth ions in the semiconductor is one of the very effective method to realize this intention. It can effectively transform near infrared light to the visible and UV light by means of a process called the upconversion [23,24]. Upconversion process is a non-linear optical effect that can be used to convert low energy incident radiation (infrared light) into higher energy emitted radiation (UV and visible light) via multiple absorption or energy transfer [25,26]. For example, Liu et al. [27]. reported that the Er^{3+} doped β-Bi_2O_3 photocatalysts showed excellent photocatalytic efficiency, and this was attributed to the doped Er^{3+}, which could effectively convert long wavelength light (e.g. IR) to short wavelength light (e.g. visible light). Other upconversion rare earth ions, such as Nd^{3+} [28], Pr^{3+} [29], Yb^{3+} [30], Tm^{3+} [31], Sm^{3+} [32], have also been utilized to dope photocatalysts.

Fig. 2. SEM images of BOI (a, b), 0.75Fe–BOI (c,d) and 4Er/0.75Fe–BOI (e, f) samples.

2.3. Photocatalytic test

The photocatalytic activities of the as-prepared samples were measured by examining the photo-degradation of organic pollutants phenol, bisphenol A (BPA) and antibiotic chloramphenicol (CAP) (The molecular structure shown in Fig. S1) under visible light irradiation at ambient temperature. A 400 W halogen lamp with 400 nm cutoff filter was employed as a visible light source. The decomposition of the pollutants were carried out with 50 mg of the catalyst dispersing uniformly into 50 mL phenol, bisphenol A, or chloramphenicol solution (phenol = 20 mg/L, BPA = 15 mg/L, CAP = 15 mg/L) in a quartz catalyst tube, respectively. Prior to irradiation, the as-prepared samples as photocatalysts for phenol, BPA, and CAP were continuously stirred in the dark for 30 min to ensure an adsorption-desorption equilibrium. During the irradiation, 2 mL of suspension was taken out at a given interval for subsequent pollutant concentration analysis by using a U-3010 UV–vis spectrophotometer. The wavelength of phenol, BPA, and CAP was detection at 270 nm, 277 nm and 278 nm, respectively.
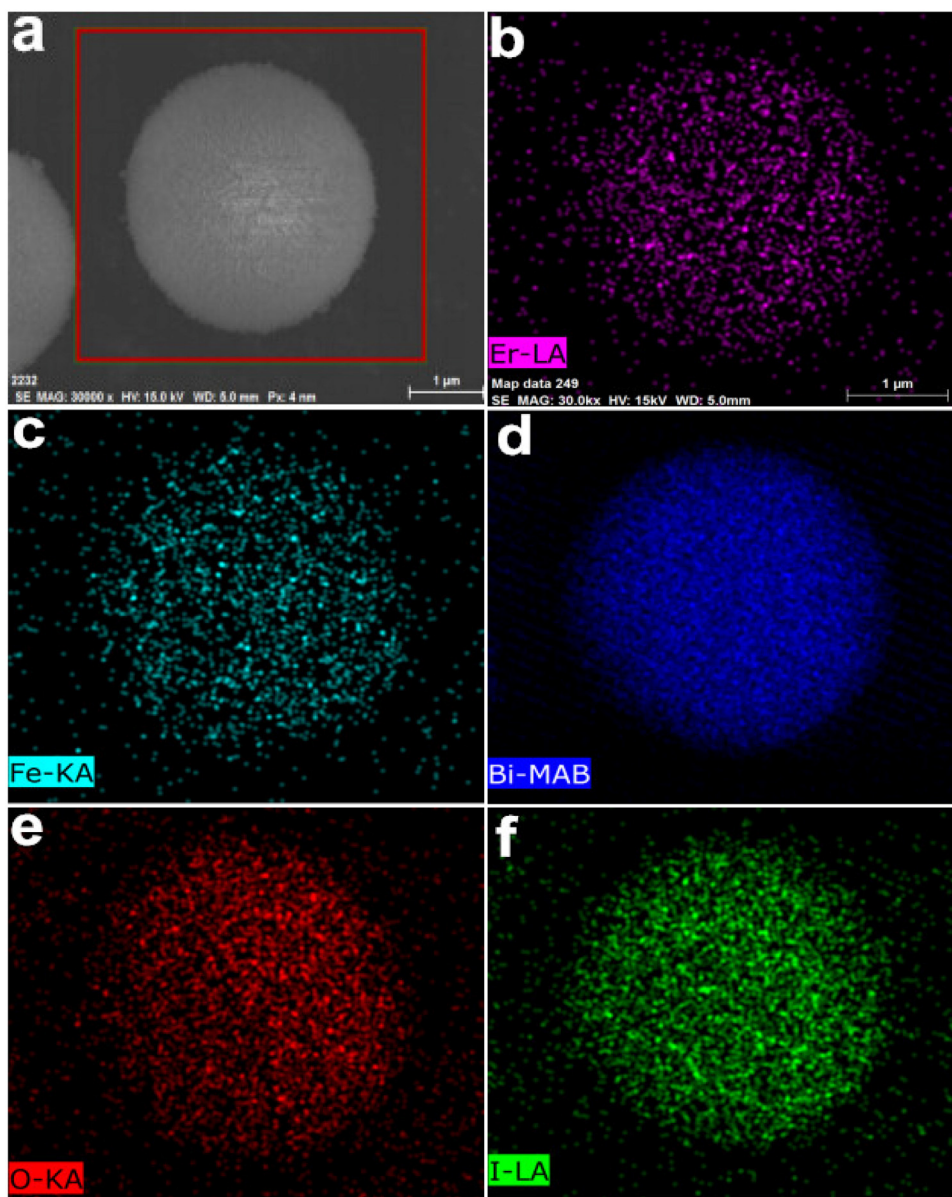
2.4. LED photo-reactor

The LED photo-reactor was wrapped with 3W LED lights (PCX50A discover, Beijing Perfect Light Technology co., LTD). Five different LED strips were used in this work, namely: blue light (B-LED, $\lambda = 450$ nm), green light (G-LED, $\lambda = 525$ nm), yellow light (Y-LED, $\lambda = 585$ nm), red light (R-LED, $\lambda = 630$ nm) and white LED (W-LED, $\lambda = 400$–780 nm). The electric current was adjusted to 0.7 A and the speed was adjusted to pass 500 r/min during the experiment. The spectral range of LED light is shown in the supporting information (Fig. S2).

3. Results and discussion

Fig. 1 shows the XRD patterns of Fe^{3+}-doped and Fe^{3+}/Er^{3+} co-doped Bi_5O_7I samples, respectively. All of the diffraction peaks in Fig. 1a can be well-indexed to orthorhombic phase Bi_5O_7I (JCPDS 40-0548). On the other hand, the as-prepared samples were well-crystallized and the doped Fe^{3+} did not change the phase structure of Bi_5O_7I. However, the phase structure of final products are transformed into monoclinic phase Bi_5O_7I (black line in Fig. 1b) with

Fig. 3. SEM image for 4Er/0.75Fe-BOI sample (a); EDS mapping images of the Er (b), Fe (c), Bi (d), O (e) and I (f) elements respectively.

a space group of C2/m (12) (JCPDS 38-0669) after the doping of Er^{3+}, and most of the signals, especially (004) peak, are widened and subdued simultaneously (Fig. 1b) when the doping amount is increased. From our perspective, this can be attributed to the doping of Fe^{3+} and Er^{3+} ions into Bi_5O_7I crystal, which will restrain the growth of Bi_5O_7I crystalline. According to the previous reported, it can be demonstrated that the presence of Er^{3+} is easy to induce the phase transformation [26,34,35].

Figs. 2 and S3 present the SEM images of the synthesized Fe^{3+}-doped and Fe^{3+}-Er^{3+} co-doped Bi_5O_7I samples. As shown in Fig. 2a, the pure Bi_5O_7I sample consists of uniform spherical porous structures, with the diameters of 2–3 μm. In Fig. 2b, the higher resolution SEM images show that these spherical porous structures were assembled by a large number of nanosheets randomly packed at the external surfaces of microspheres. Fig. 2c–e shows the SEM images of 0.75Fe-BOI and 4Er/0.75Fe-BOI samples, respectively. There are no significant change on the morphology after Fe^{3+}/Er^{3+}-doping. However, as shown in Figs. 2 and S3, the thickness of the sheets in the microspheres was decreased after being doped with Er^{3+}, which are in agreement with the XRD results in Fig. 1b. The EDS elemental

Table 1
Properties of the 0.75Fe-doped and 0.75Fe-Er co-doped Bi_5O_7I samples.

Sample	Atomic% of dopant from ICP-MS		Band gap (eV)
	Fe	Er	
0.75Fe–BOI	0.72	–	2.38
2Er/0.75Fe-BOI	0.69	1.93	2.34
4Er/0.75Fe-BOI	0.70	3.92	2.31
6Er/0.75Fe-BOI	0.73	5.89	2.21
8Er/0.75Fe-BOI	0.68	7.91	2.16

mapping was selected for the further analysis of elemental distribution in the 4Er/0.75Fe-BOI sample. As shown in Fig. 3b–f, the Er, Fe, Bi, O, and I elements were well distributed in the microsphere. Moreover, ICP-MS analyses were performed in order to estimate the total average dopant concentrations in 0.75Fe-doped and 0.75Fe-Er co-doped Bi_5O_7I samples. As shown in Table 1, it was observed that the final resulting amount of Fe or Er in the doped materials was

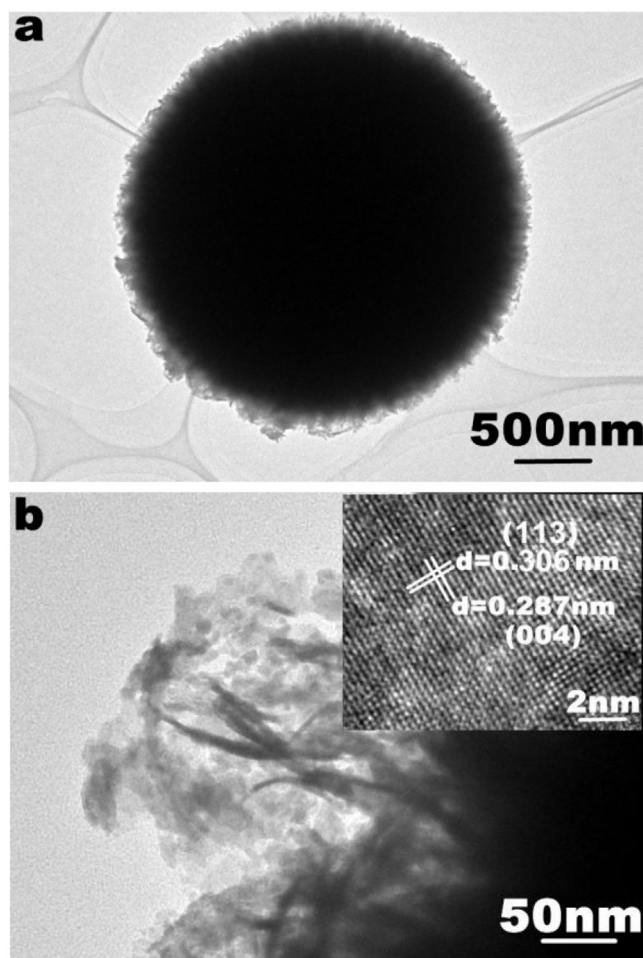**Fig. 4.** TEM (a) and HRTEM (b) images of 4Er/0.75Fe-BOI sample.

Fig. 5. High-resolution XPS spectra of Fe 2p (a) and Er 4d (b) of 4Er/0.75Fe-BOI sample.

a little lower than the expected one, which due to an intrinsic loss during the solvothermal synthesis processes.

The microstructures and morphologies details of the 4Er/0.75Fe-BOI sample were further investigated by the TEM and HRTEM. Fig. 4a shows the 4Er/0.75Fe-BOI sample revealing with well-defined porous spherical nanostructure, and the sphere diameters is around 3 μm. Fig. 4b shows that the surface of the sphere is fully covered by ultrathin nanosheets with the thickness of ∼5 nm. The HRTEM image inset in Fig. 4b shows that two different lattice fringes with the spacings of $d = 0.287$ nm and $d = 0.306$ nm, which are ascribed to the (004) and (113) crystallographic planes of monoclinic Bi_5O_7I, respectively.

The surface elemental composition and chemical states of 4Er/0.75Fe-BOI were analyzed by XPS (Figs. S4 and 5). The XPS survey spectrum in Fig. S4a indicates that the sample contains only Bi, O, I, C, Fe, and Er. The C 1s peak is attributed to the signal from contamination carbon on the sample surface. The two peaks at 159.1 and 164.3 eV (Fig. S4b) are attributed to the binding energies of Bi $4f_{7/2}$ and Bi $4f_{5/2}$ [36], respectively. The O 1s spectra of 4Er/0.75Fe-BOI sample shown in Fig. S4c can be deconvoluted by two symmetric Gaussian curves, which are attributed to the oxygen in the BOI crystal lattice (529.8 eV), and surface chemisorbed oxygen (531.9 eV) [37], respectively. The peaks in 619.3 and 630.7 eV (Fig. S4d) belong to the I $3d_{5/2}$ and I $3d_{3/2}$ [38], respectively. XPS signals of Fe 2p (Fig. 5a) were observed at binding energies of ∼711 and 724 eV, which can be assigned to Fe $2p_{3/2}$ and Fe $2p_{1/2}$ for the ferric (III) ions [39]. As shown in Fig. 5b, it can be seen that the Er 4d peak is observed at binding energies of ∼169.6 eV, which is in
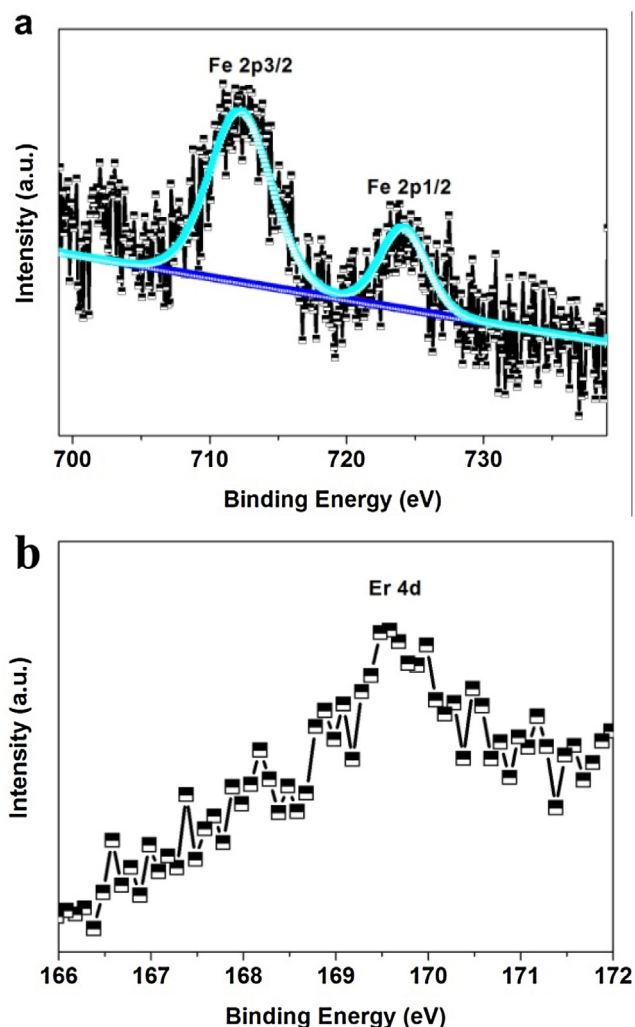
agreement with the Er^{3+} in previous reported [40]. From the above results, it can be concluded that the Fe^{3+} ions and Er^{3+} ions were successfully incorporated into BOI sample.

The specific surface areas (S_{BET}) of BOI, 0.75Fe-BOI and 4Er/0.75Fe-BOI photocatalysts were measured by N_2 adsorption-desorption analysis. Fig. 6 shows the corresponding N_2 adsorption-desorption isotherms for BOI, 0.75Fe-BOI, and 4Er/0.75Fe-BOI, respectively. The isotherms of all the photocatalysts are of typical type-IV with H1 hysteresis. According to IUPAC classification, this feature is the symbol of the typical mesoporous structure. In the inset of Fig. 6, the pore size distribution curves are calculated from the desorption branches of the isotherms via the Barrett-Joyner-Halenda (BJH) method, and it reveals that all the samples have a pore diameter in the range of 2.0–60.0 nm. By using the N_2 adsorption-desorption isotherms, the surface area values are calculated as 16.16, 17.23, and 22.98 m^2/g for BOI, 0.75Fe-BOI, and 4Er/0.75Fe-BOI, respectively. It can be found that the surface area of the samples increased after being doped with the Fe^{3+} and Er^{3+}, and this result is beneficial to the photocatalytic activities of photocatalysts [41].

Fig. 7 a and b shows the UV–vis diffuse reflectance spectra of all the samples. The pure BOI exhibits an optical response wavelengths shorter than 450 nm, which indicates that the pure BOI sample can be excited by UV light and by a small part of visible light. The doping process could lead to a remarkable red shift for
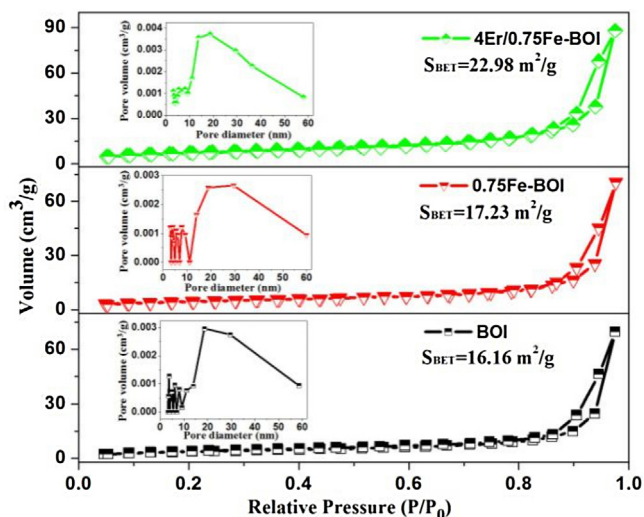
Fig. 6. N_2 adsorption-desorption isotherms of BOI, 0.75Fe-BOI and 4Er/0.75Fe-BOI; inset of pore size distribution.

absorption edge of Fe-BTO, and the absorption of visible light region was extended (400–550 nm) after Fe^{3+}-doping, as compared with pure BOI. As shown in Fig. 7b, the results of BOI and 0.75Fe-BOI indicate that further introduction of Er^{3+} can cause a significant

red shift of absorption edge to the visible light region, and three absorption peaks centered at 523, 654, and 796 nm were observed for Er^{3+} doped 0.75Fe-BOI. This could be assigned to the upconversion energy transitions from the $^4I_{15/2}$ ground state to $^2H_{2/11}$, $^4F_{9/2}$, and $^4I_{9/2}$ states of Er^{3+}, respectively [42,43]. Evidently, the optical absorption near the band edge follows the T_{auc} equation:

$$\alpha h\nu = A(h\nu - E_g)^{n/2} \tag{1}$$

For semiconductor, the square of absorption coefficient is usually linear with energy ($h\nu$) in the absorption edge region during the direct optical transition progress. The plots of $(\alpha h\nu)^{1/2}$ versus energy ($h\nu$) is shown inset in Fig. 7(a, b). The E_g values of the pure BOI, 0.5Fe-BOI, 0.75Fe-BOI, 1.0Fe-BOI, 1.5Fe-BOI, 4Er-BOI, 4Er/0.75Fe-BOI and 8Er-0.75Fe-BOI samples can be calculated in the range of 2.04–2.85 eV and listed in Table 1.

In order to clarify how the Fe^{3+}-doping affects the absorption spectra of BOI crystal, the electronic structures of pure and Fe^{3+}-doping BOI crystals were calculated by DFT method. The density of states (DOS) of pure BOI and Fe^{3+}-doping BOI crystals are shown in Fig. 7c and b. For BOI (Fig. 7c), the states in the valence band region from −6 to 0 eV are mainly composed of the O 2p, I 2p, Bi 6s, and Bi 6p orbital; however, I 2s and O 2p are closer to Fermi level and contribute more electrons. The conduction band is made up with the I 2p, O 2p, Bi 6s, and Bi 6p orbital, and the Bi 6p contributes more electrons. After the introduction of Fe^{3+} (Fig. 7d), it results in the shift of the Fermi level (E_f) and facing with the minimum
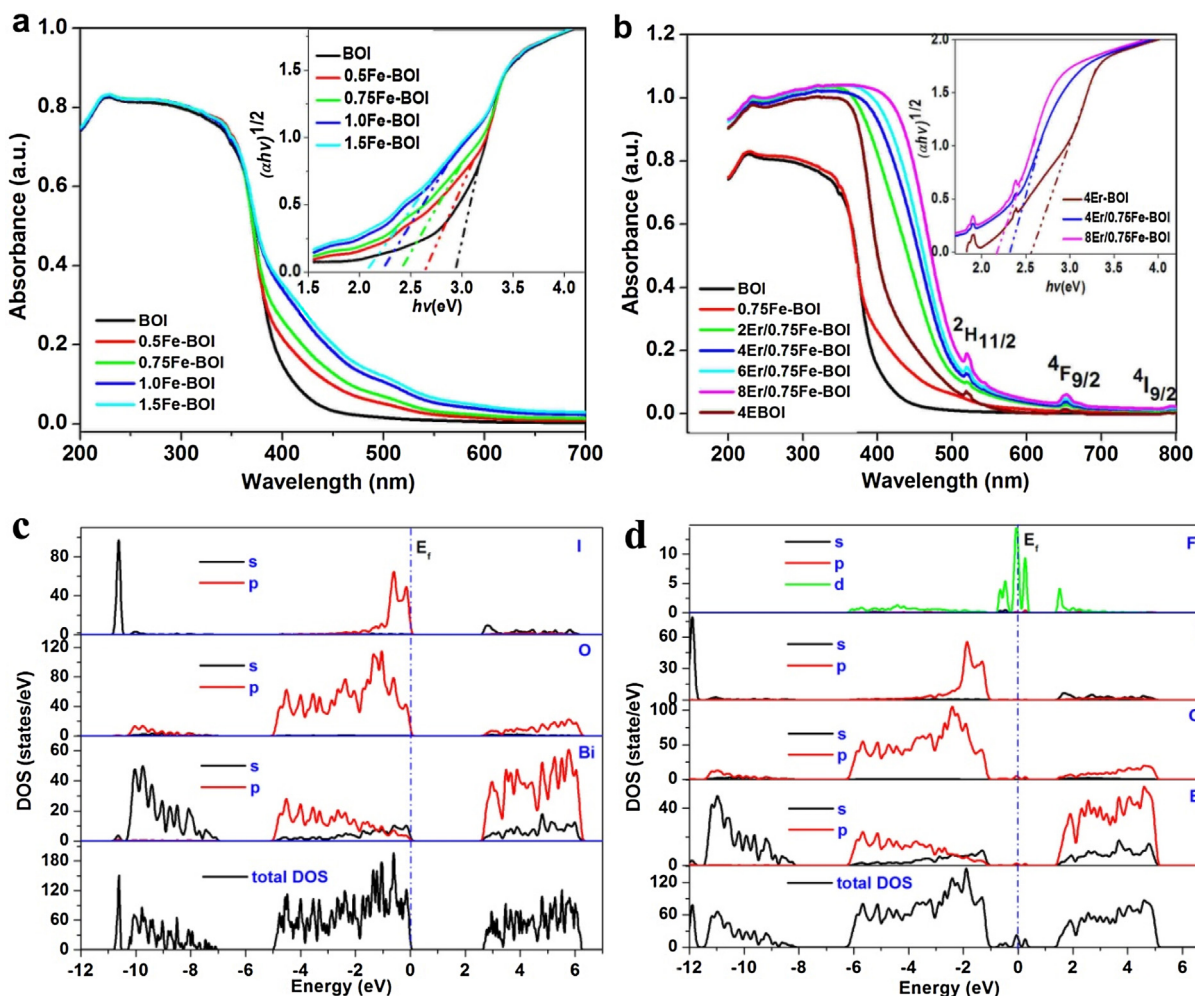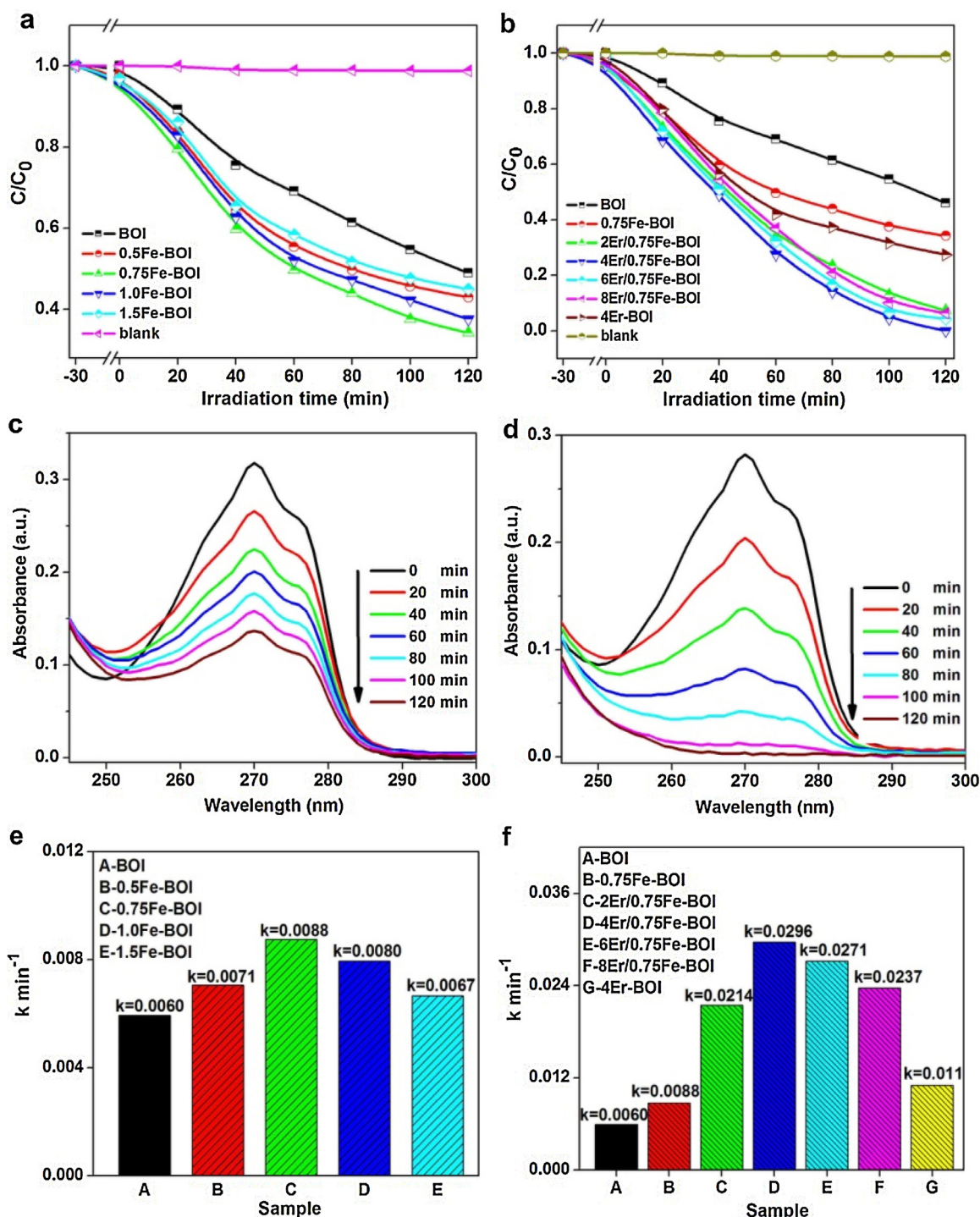

Fig. 7. UV–vis adsorption spectra of synthesized Fe^{3+}-doped (a) and Fe^{3+}-Er^{3+} co-doped (b) Bi_5O_7I photocatalysts, inset the plots of $(\alpha h\nu)^{1/2}$ versus energy ($h\nu$) of Fe^{3+}-doped Bi_5O_7I; The density of states (DOS) of pure BOI (c) and Fe^{3+}-doped BOI (d) crystals.

Fig. 8. Variation of phenol concentration (C/C_0) against photo-degradation time for pure BOI and Fe-doped BOI (a) and variation of phenol concentration (C/C_0) against photo-degradation time for (b); time-dependent UV–vis spectra of phenol solution for BOI (c) and 4Er/0.75Fe-BOI sample (d). $ln(C_0/C_t)$ and irradiation time (t) of Fe-BOI (e) and Er/Fe-BOI (f).

conduction-band; hence, generates a defect state within the band gap of the perfect BOI. To compare with the pure BOI, the electronic structures of Fe^{3+}-doped BOI include with impurity state and localized Fe 3d band existed in the middle of the Fe^{3+}-doped BOI band gap. Moreover, the conduction band is consisted of Fe 3d + O 2p + Bi 6p + I 2s hybrid orbital instead. The band structure indicates that charge transfer upon photoexcitation occurs from the Fe 3d to the empty Fe 3d + Bi 6p hybrid orbital. The band gap of pure BOI is estimated to be 2.72 eV (shown in Fig. S5a) which is slightly smaller

than UV–vis spectra results (2.85 eV). Usually, the band gap calculated by DFT is smaller than that by experimental results [44]. The band gap of Fe^{3+}-doped BOI is estimated to be 1.21 eV (shown in Fig. S5b), which is much more narrow than that of BOI (2.85 eV). This result is consistent with the red-shift in UV–vis spectra in Fig. 7a.

The photocatalytic activity of pure BOI and Fe^{3+}-doped BOI photocatalysts was first evaluated by the photo-degradation of phenol under visible light irradiation. Fig. 8a shows the relationship of phenol concentration (C/C_0) and irradiation time for
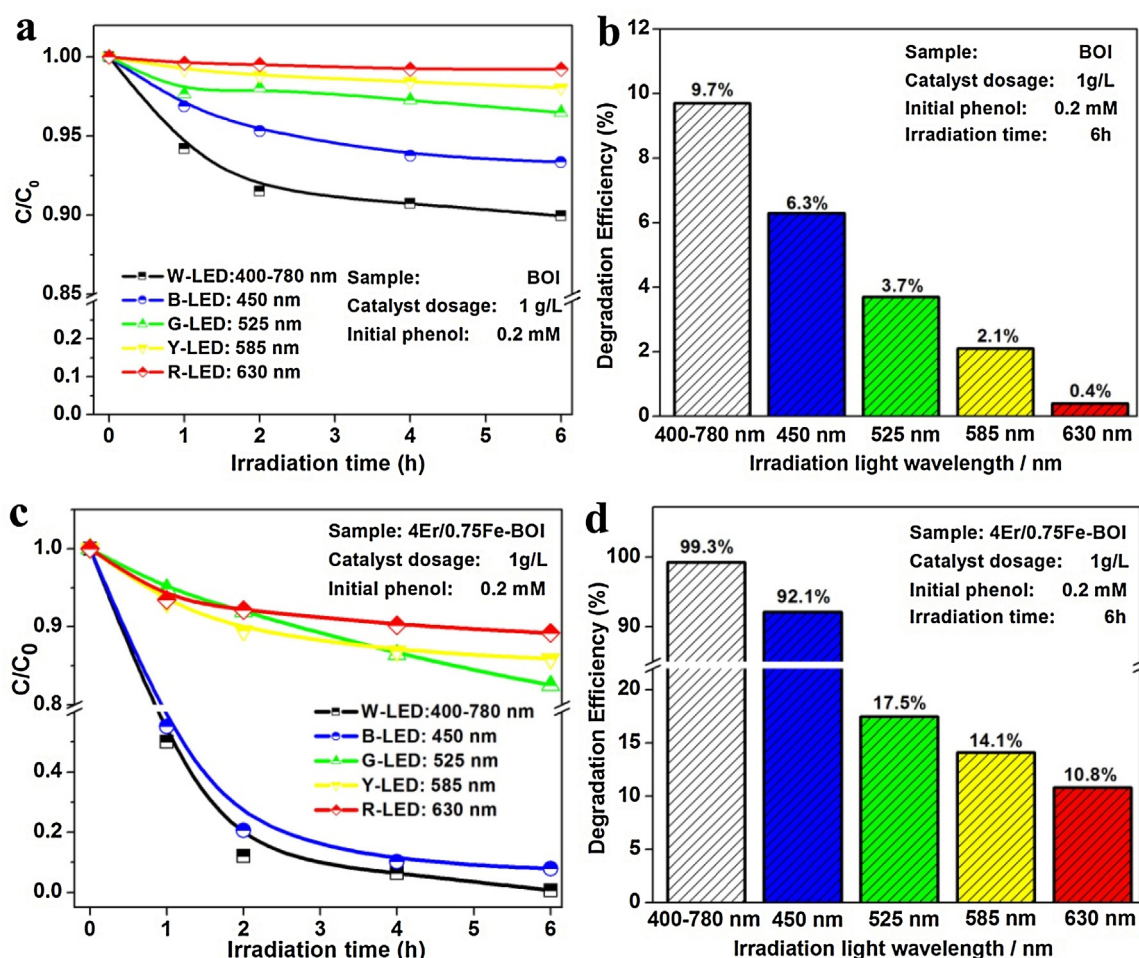
Fig. 9. The photocatalytic activities of the pure BOI (a, b) and 4Er/0.75Fe-BOI (c, d) sample under irradiation of different wavelength monochromatic light.

different samples. 0.75Fe-BOI exhibits the highest photocatalytic activity among all the samples. After 120 min irradiation, the photo-degradation rates of phenol for pure BOI, 0.5Fe-BOI, 0.75Fe-BOI, 1.0Fe-BOI, and 1.5Fe-BOI reached 51.1%, 56.1%, 64.3%, 60.9%, and 53.6%, respectively. Furthermore, phenol was also chosen to fur-ther examine the photocatalytic activity of these photocatalysts (Fig. 8b). Under the visible light irradiation, 4Er/0.75Fe-BOI photo-catalysts (blue line in Fig. 8b) shows the best photocatalytic activity for the degradation of phenol. After 120 min photo visible light irradia-tion, the photodegradation rates of 51.1%, 64.3%, 92.4%, 100%, 95.6%, 93.5%, and 72.5% are obtained for BOI, 0.75Fe-BOI, 2Er/0.75Fe-BOI, 4Er/0.75Fe-BOI, 6Er/0.75Fe-BOI, 8Er/0.75Fe-BOI and 4Er-BOI, respectively. The UV–vis spectral of phenol are presented in Fig. 8(c) and (d) respectively, which describe the changing of the phenol in aqueous solution over pure BOI and 4Er/0.75Fe-BOI photocatalysts under different duration of visible light irradiation. The intensity of the maximum absorption peak, at 270 nm, decreases dramat-ically as irradiation time increases, and the absorption peak in the 4Er/0.75Fe-BOI system becomes completely disappeared after 120 min.
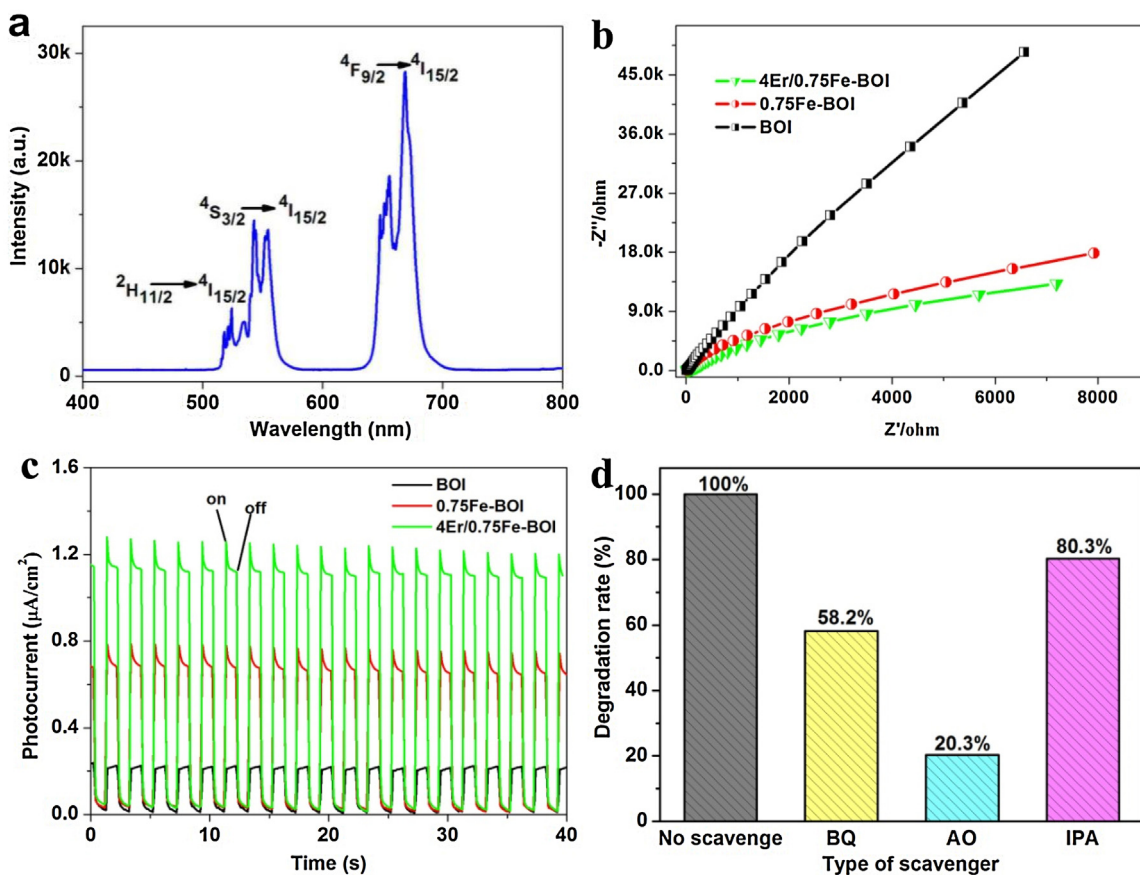
To understand the reaction kinetics of phenol under visible light irradiation, the experimental data of photocatalytic activity test were fitted with the pseudo-first-order model, and the photo-degradation rate was evaluated by the pseudo-first-order kinetic constant k (as shown in Fig. S6) [45]. According to Fig. 8e, the k of the as-prepared BOI and Fe^{3+}-doped BOI samples were calculated to be 0.0060, 0.0071, 0.0088, 0.0080, and 0.0067 min^{-1}, respectively. The results indicate that Fe^{3+} doping has greatly improved the pho-

tocatalytic activity on degrading phenol. As shown in Fig. 8f, the pseudo-first-order reaction rate constants k_1 are 0.0060, 0.0088, 0.011, 0.0214, 0.0296, 0.0271, and 0.0237 min^{-1} for the as-prepared BOI, 0.75Fe-BOI, 4Er-BOI, and n% Er^{3+}-doped 0.75Fe-BOI (n = 2–8) samples, respectively. It is found that the degradation rate constant for phenol by 4Er/0.75Fe-BOI is more than 4, 3, and 2.6 times higher than that by pure BOI, 0.75Fe-BOI, and 4Er-BOI, respectively. The kinetics study of the phenol degradation for pure BOI, 0.75Fe-BOI, and 4Er/0.75Fe-BOI proved the synergism effect of Fe^{3+} and Er^{3+} in the 4Er/0.75Fe-BOI photocatalysts.

As shown in Fig. S2, the wavelength range of LED light is 400–800 nm, and the intensity of those monochromatic light is quite different. The influence of the monochromatic light on the photocatalytic activity of pure BOI and 4Er/0.75Fe-BOI (Fig. 9) were also investigated. The results show that only 9.7% phenol was degraded under white light irradiation for 6 h by BOI, and the degradation efficiency under red light irradiation are negligi-ble. However, the degradation efficiencies of 99.3%, 92.1%, 17.5%, 14.1%, and 10.8% (Fig. 9c, d) under white (W), blue (B), green (G), yellow (Y), and red (R) light irradiation for 6 h are obtained by 4Er/0.75Fe-BOI. Obviously, the photocatalytic activity of 4Er/0.75Fe-BOI sample was greatly improved. More interest-ingly, the 4Er/0.75Fe-BOI exhibits photocatalytic activity beyond the absorption edge (shown in Fig. 7). The reason will further inves-tigated in the following results.

Under the identical experimental conditions, BOI, 0.75Fe-BOI, 4Er-BOI, and 4Er/0.75Fe-BOI were also selected to further inves-tigate the photocatalytic activity for other two kinds of colorless

Fig. 10. Upconversion spectra of 4Er/0.75Fe-BOI sample under the excitation at 980 nm laser (a); electrochemical impedance spectroscopy of pure BOI, 0.75Fe-BOI and 4Er/0.75Fe-BOI samples (b) and transient photocurrent responses (c); and the effect of different quenchers for the photocatalytic activities under visible light irradiation (d).

model contaminants, i.e., bisphenol A (BPA) and chloramphenicol (CAP). The results show that the 4Er/0.75Fe-BOI (Figs. S8 and S9) also exhibited a superior activity for the removal of the organic pollutant BPA and CAP from aqueous solution during photodegradation processes under visible light irradiation. The kinetics study (Fig. S8) of the BPA and CPA degradation over BOI, 0.75Fe-BOI, 4Er-BOI, and 4Er/0.75Fe-BOI under visible light irradiation are generally evidence the synergism of Fe^{3+} and Er^{3+} doping in the 4Er/0.75Fe-BOI, especially the photocatalytic degradation for CPA.

In order to improve solar energy utilization, effectively using not only UV and visible lights, but also NIR light, are required to enhance the photocatalytic activity. Many studies have been reported by doping with Er^{3+} into the semiconductors, and the resulting photocatalysts always show better photocatalytic activity through an up-conversion mechanism [25–27,30,31]. Fig. 10a shows that the up-conversion of 4Er/0.75Fe-BOI powders can be excited by a NIR diode laser light ($\lambda = 980$ nm), and green and red light with different intensity were emitted, with the emission peaks at approximately 525, 542, and 668 nm. The green emissions between 517–537 nm and 537–560 nm are attributed to the $^2H_{11/2} \rightarrow {}^4I_{15/2}$ and $^4S_{3/2} \rightarrow {}^4I_{15/2}$ transitions, respectively. A dominant red emission is observed between 644–680 nm, which is due to the transition from $^4F_{9/2}$ to $^4I_{15/2}$. Therefore, the NIR light can be utilized by the way of up-conversion over the as-prepared 4Er/0.75Fe-BOI sample.

It is well known that the photocatalytic process using semiconductor involves light photoexcitation, the subsequent separation and transfer of photogenerated charge carriers, and the final redox reactions between the charge carriers and adsorbate on the semiconductor surface. Accordingly, the charge dynamics property

plays an important role in determining the ultimate photoreactivity. The separation and transfer of photogenerated charge carriers in the pure BOI, 0.75Fe-BOI, and 4Er/0.75Fe-BOI samples were investigated by photoluminescence (PL) emission and electrochemical impedance spectroscopy (EIS) as well as transient photocurrent responses. The results of room-temperature PL spectra (Fig. S7) and the Nyquist plot diameter (Fig. 10b) show that doping with Fe^{3+} and Er^{3+} favors the separation and transfer efficiency of photogenerated electron-hole pairs in the 4Er/0.75Fe-BOI sample. Transient photocurrent responses in Fig. 10c was further conformed when Er^{3+}/Fe^{3+} was doped into the BOI catalyst, which leads to e^-/h^+ charge separation, and hence reduces the combination rate. Thus, the results also indicated that Er^{3+}/Fe^{3+} co-doped BOI will be an effective catalyst compared to pure BOI and Fe^{3+} doped samples.

In the photocatalytic oxidation process of organic pollutants, there are series of photoinduced reactive species, including $^\bullet OH$, $O_2^{\bullet -}$, h^+, etc. These species will be directly involved in the process when the electron-hole pairs are generated under visible light irradiation [46]. In order to evaluate how different reactive species play their role in contaminant degradation, the quenchers of ammonium oxalate (AO), isopropyl alcohol (IPA), and benzoquinone (BQ) were used to scavenge the relevant reactive species during the photodegradation of phenol by 4Er/0.75Fe-BOI under visible light irradiation. In this work, AO (1.0 mmol/L), IPA (1.0 mmol/L), and BQ (1.0 mmol/L) were adopted as hole (h^+), hydroxyl radicals ($^\bullet OH$), and superoxide anions ($O_2^{\bullet -}$) scavengers, respectively, and the corresponding results are shown in Fig. 10d. With the addition of AO and BQ, only about 20.3% and 58.2% of phenol was degraded under visible light irradiation. The above results suggested that both h^+
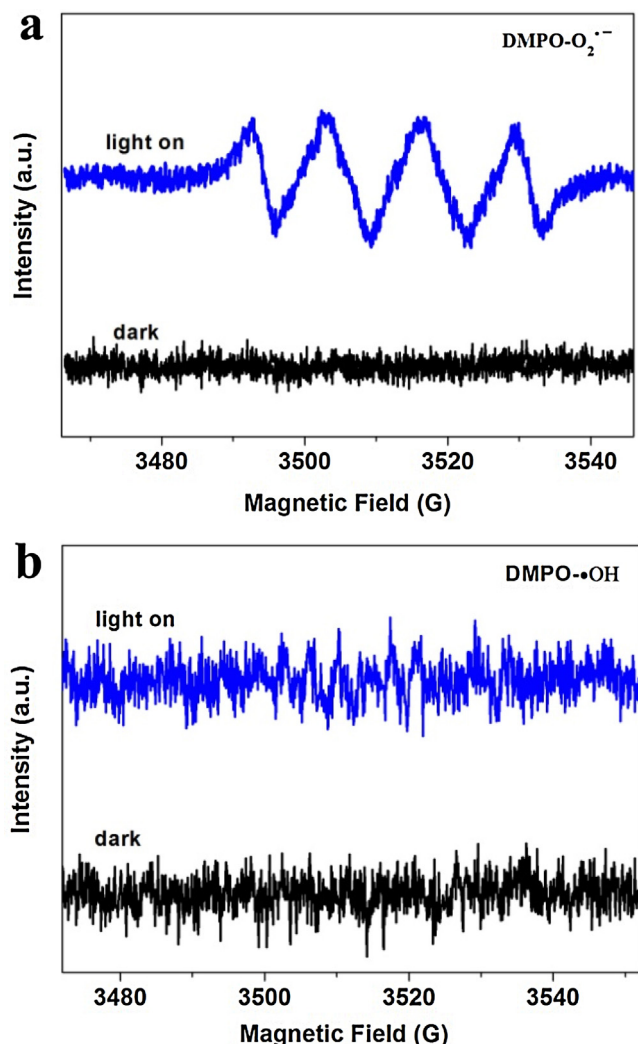
a

DMPO-O$_2$$^{•−}$

light on

dark

b

DMPO-$^•$OH

light on

dark

Fig. 11. ESR spectra of 4Er/0.75Fe-BOI in methanol dispersion for DMPO-O$_2$$^{•−}$ (a) and in aqueous dispersion for DMPO-$^•$OH (b) under visible light irradiation.
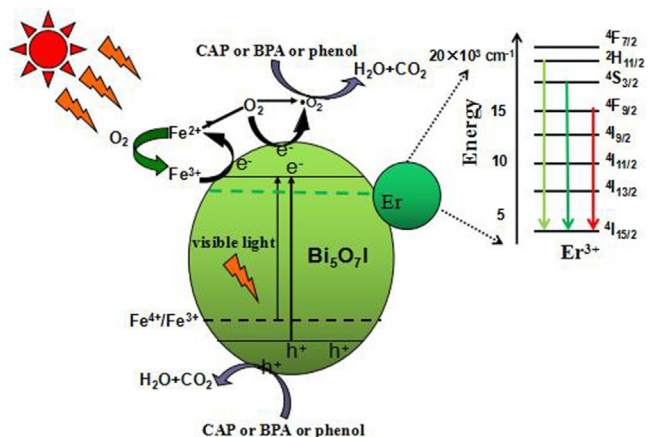

Fig. 12. Schematic photodegradation mechanisms over 4Er/0.75Fe-BOI sample under visible light irradiation.

and O$_2$$^{•−}$ species, especially the former, play important role in the photo-degradation of phenol over the 4Er/0.75Fe-BOI under visible light irradiation. In order to further investigate the reactive species responsible for photocatalytic degrade of phenol under visible light irradiation, the electron spin resonance (ESR) spin-trap with DMPO technique was employed to detect the reactive over 4Er/0.75Fe-BOI under dark and visible light irradiation. As shown in Fig. 11a, it could be clearly seen that the signals of DMPO-O$_2$$^{•−}$ under visible light irradiation and no such signals detected in dark. However, the characteristic signals corresponding to the DMPO-$^•$OH adduct (as shown in Fig. 11b) did not appeared under the visible light irradiation or under dark. The ESR results indicate that the O$_2$$^{•−}$ radicals were produced during the photocatalytic process, while no $^•$OH radicals can be generated in this system, which are well consistent with the active species trapping experimental results in Fig. 10d.

From the above results, 4Er/0.75Fe-BOI shows a high photocatalytic activity for photo-degradation of phenol under visible light irradiation, and the possible mechanisms for the enhancement in photocatalytic activity is shown in Fig. 12. Firstly, the above TEM and BET results (Figs. 4 and 6) show that porous 4Er/0.75Fe-BOI microspheres were constructed by ultrathin nanosheets and presented with high specific surface area. This can provide more reaction sites and benefit the photocatalytic process [47]. Secondly, the upconversion reagent Er^{3+} has abundant energy levels in the

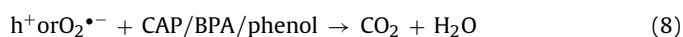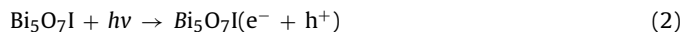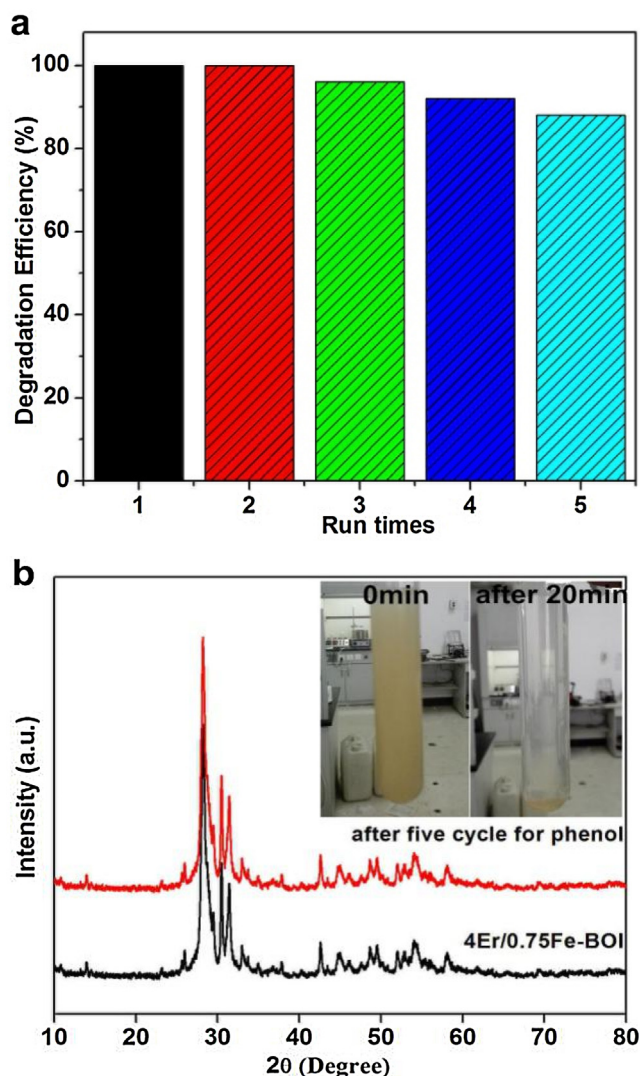IR-UV range, which can be easily excited by solar light [48,49]. Furthermore, the doping of Er^{3+} will result in new energy-band in Bi$_5$O$_7$I that acts as a scavenger to capture photogenerated electrons, enhancing the electron-hole separation [31]. Moreover, Er^{3+} could also be reduced to Er^{2+} by trapping an electron from the valence band (Bi$_5$O$_7$I), while release the corresponding movable holes. In this case, Er^{2+} would react with O$_2$ to form active superoxide radicals (O$_2$$^{•−}$) species, which induces charge carrier separation to inhibit the recombination of electrons and holes [50]. Meanwhile, the reactive species (h$^+$ and O$_2$$^{•−}$) that formed on the surfaces of Er^{3+}-doped Bi$_5$O$_7$I, can participate in the photocatalytic reaction. Thirdly, the doped Fe^{3+} can turn into Fe^{2+} and Fe^{4+} ions by trapping photogenerated electrons and holes respectively, holding up the recombination process. However, the Fe^{2+} and Fe^{4+} ions have half-filled 3d^5 orbital and become relatively unstable than the Fe^{3+} ions. Therefore, the trapped charges can easily release from Fe^{2+} or Fe^{4+} ions and then migrate to the surface to initiate the photocatalytic reaction. Fe^{2+} ions can be oxidized to Fe^{3+} ions by transferring electrons to absorbed O$_2$ on the surface of Bi$_5$O$_7$I and the adsorbed O$_2$ is reduced to superoxide radical. Meanwhile, Fe^{4+} ions are also reduced to Fe^{3+} ions by releasing electrons [15,16]. The trapped holes can also contribute to the degradation of phenol in solution. Finally, the synergy of Er^{3+} and Fe^{3+} codoped Bi$_5$O$_7$I with doping mechanism and upconversion luminescence property would further improve the photocatalytic activity. The detailed photodegradation reaction processes are as follows:

$$Bi_5O_7I + h\nu \rightarrow Bi_5O_7I(e^- + h^+) \tag{2}$$

$$Fe^{3+} + e^- \rightarrow Fe^{2+} \tag{3}$$

$$Fe^{2+} + O_2 \rightarrow Fe^{3+} + O_2^{•-} \tag{4}$$

$$O_2 + Fe^{3+} + e^- \rightarrow Fe^{2+} \tag{5}$$

$$Fe^{3+} + h^+ \rightarrow Fe^{4+} \tag{6}$$

$$Fe^{4+} + e^- \rightarrow Fe^{3+} \tag{7}$$

$$h^+ or O_2^{•-} + CAP/BPA/phenol \rightarrow CO_2 + H_2O \tag{8}$$

In order to investigate the stability and recyclability of the as-synthesized 4Er/0.75Fe-BOI microspheres for the photocatalytic degradation of phenol, the 4Er/0.75Fe-BOI powders were reused five times under the same reaction conditions (the initial concentration was 20 mg/L) and the results shown in Fig. 13a. After five cycles, the 4Er/0.75Fe-BOI sample still retains a relatively high photocatalytic performance for the degradation of phenol and the photo-degradation rate is 88%, after 120 min irradiation. The decreased photocatalytic performance may be due to mass loss

Fig. 13. Reusability of the 4Er/0.75Fe-BOI photocatalyst after five runs for the photocatalytic degradation of phenol under visible light irradiation (a) and XRD patterns of 4Er/0.75Fe-BOI sample after five cycles for phenol (b); inset shown the solutions photographs of 4Er/0.75Fe-BOI catalyst before and after sedimentation for 20 min.

during the sedimentation and transferring processes. The XRD patterns (Fig. 13b) of the 4Er/0.75Fe-BOI sample before and after the photocatalytic reactions with phenol aqueous solution show that the structure and phase remained unchanged after the photocatalytic reactions. The results shown in the inset of Fig. 13b indicate that the 4Er/0.75Fe-BOI photocatalysts can be easily separated from aqueous suspension by sedimentation. Therefore, the 4Er/0.75Fe-BOI catalysts shows a highly efficient photocatalytic activity for the degradation of organic pollutants under visible light irradiation and outstanding recyclability, which would have great potential in practical applications in the future.

4. Conclusions

Uniform porous Bi_5O_7I microspheres photocatalysts co-doped with Fe^{3+} and Er^{3+} were synthesized by combining the hydrothermal synthesis with thermal treatment method. The novel Er^{3+}/Fe^{3+} codoped Bi_5O_7I photocatalysts achieved the synergistic effects of narrowed band gap and enhanced e^-/h^+ separation (Fe^{3+} or Er^{3+}-doping), and efficient use of NIR light by up-conversion property (Er^{3+}-doping). As such, it showed a remarkably enhanced photo-catalytic activities for degradation of phenol, BPA, and CAP under visible light irradiation, as compared with the pure Bi_5O_7I. Moreover, the as prepared Er^{3+}/Fe^{3+} codoped BOI photocatalyst also showed good photostability under visible light and high recyclability in the degradation of phenol in aqueous solution, which have great potential in practical applications in the future.

Acknowledgements

Appendix A. Supplementary data

Supplementary data associated with this article can be found, in the online version, at http://dx.doi.org/10.1016/j.apcatb.2016.12.061.

References

[1] Q.Z. Wang, J.H. Lian, J.J. Li, R.F. Wang, H.H. Huang, B.T. Su, Z.Q. Lei, Highly efficient photocatalytic hydrogen production of dlowerlike cadmium sulfide decorated by histidine, Sci. Rep. 5 (2015) 13593–13602.
[2] L.Q. Ye, Y.R. Su, X.L. Jin, H.Q. Xie, C. Zhang, Recent advances in BiOX (X = Cl, Br and I) photocatalysts: synthesis modification, facet effects and mechanisms, Environ. Sci.: Nano 1 (2014) 90–112.
[3] G.Q. Zhu, Y.B. Liu, M. Hojamberdiev, J.L. Han, J. Rodriguez, S.A. Bilmes, P. Liu, Thermodecomposition synthesis of porous β-Bi₂O₃/Bi₂O₂CO₃ heterostructured photocatalysts with improved visible light photocatalytic activity, New J. Chem. 39 (2015) 9557–9568.
[4] C.W. Tan, G.Q. Zhu, M. Hojamberdiev, K. Okada, J. Liang, X.C. Luo, P. Liu, Y. Liu, Co₃O₄ nanoparticles-loaded BiOCl nanoplates with the dominant {001} facets: efficient photodegradation of organic dyes under visible light, Appl. Catal. B: Environ. 152–153 (2014) 425–436.
[5] Z.L. Ni, Y.J. Sun, Y.X. Zhang, F. Dong, Fabrication, modification and application of (BiO)₂CO₃-based photocatalysts: a review, Appl. Surf. Sci. 365 (2016) 314–335.
[6] J. Zhang, Z.P. Zhu, Y.P. Tang, X.L. Feng, Graphene encapsulated hollow TiO₂ nanospheres: efficient synthesis and enhanced photocatalytic activity, J. Mater. Chem. A 1 (2013) 3752–3756.
[7] J.P. Wang, Z.Y. Wang, B.B. Huang, Oxygen vacancy induced band-Gap narrowing and enhanced visible light photocatalytic activity of ZnO, ACS Appl. Mater. Interfaces 4 (2012) 4024–4030.
[8] H.J. You, R. Liu, C.C. Liang, S.C. Yang, F. Wang, X.G. Lu, B.J. Ding, Tube-like ternary α-Fe₂O₃@SnO₂@Cu₂O sandwich heterostructures: synthesis and enhanced photocatalytic properties, J. Mater. Chem. A 1 (2013) 4097–4104.
[9] A.L. Linsebigler, G. Lu, J.T. Yates, Photocatalysis on TiO₂ surfaces: principles, mechanisms, and selected results, Chem. Rev. 95 (1995) 735–758.
[10] H. Tong, S.X. Ouyang, Y.P. Bi, N. Umezawa, M. Oshikiri, J.H. Ye, Nano-photocatalytic materials: possibilities and challenges, Adv. Mater. 24 (2012) 229–251.
[11] A. Zaleska, Doped-TiO₂: a review, Recent Pat. Eng. 2 (2008) 157–164.
[12] M.A. Rauf, M.A. Meetani, S. Hisaindee, An overview on the photocatalytic degradation of azo dyes in the presence of TiO₂ doped with selective transition metals, Desalination 276 (2011) 13–27.
[13] K. Wilke, H.D. Breuer, The influence of transition metal doping on the physical and photocatalytic properties of titania, J. Photochem. Photobiol. A Chem. 121 (1999) 49–53.
[14] P. Ciesla, P. Kocot, P. Mytych, Z. Stasicka, Homogeneous photocatalysis by transition metal complexes in the environment, J. Mol. Catal. A Chem. 224 (2004) 17–33.
[15] L.G. Devi, S.G. Kumar, B.N. Murthy, N. Kottam, Influence of Mn²⁺ and Mo⁶⁺ dopants on the phase transformations of TiO₂ lattice and its photocatalytic activity under solar illumination, Catal. Commun. 10 (2009) 794–798.
[16] C.J. Huang, J.L. Hua, S. Cong, Z.G. Zhao, X.Q. Qiu, Hierarchical BiOCl microflowers with improved visible-light-driven photocatalytic activity by Fe(III) modification, Appl. Catal. B: Environ. 174–175 (2015) 105–112.
[17] T. Harifi, M. Montazer, Fe³⁺:Ag/TiO₂ nanocomposite: synthesis characterization and photocatalytic activity under UV and visible light irradiation, Appl. Catal. A: Gen. 473 (2014) 104–115.
[18] J. Liang, G.Q. Zhu, Synthesis and characterization of Fe-doped β-Bi₂O₃ porous microspheres with enhanced visible light photocatalytic activity, Superlattice Microstruct. 72 (2014) 272–282.

[19] S. Chala, K. Wetchakun, S. Phanichphant, Enhanced visible-light-response photocatalytic degradation of methylene blue on Fe-loaded $BiVO_4$ photocatalyst, J. Alloy Compd. 597 (2014) 129–135.

[20] M. Nussbaum, N. Shaham-Waldmann, Y. Paz, Synergistic photocatalytic effect in Fe, Nb-doped BiOCl, J. Photochem. Photobiol. A Chem. 290 (2014) 11–21.

[21] X.H. Wu, W. Qin, L. Li, Y. Guo, Z.Y. Xie, Photocatalytic property of nanostructured Fe^{3+}-doped Bi_2O_3 films, Catal. Commun. 10 (2009) 600–604.

[22] S. Guo, X.F. Li, H.Q. Wang, Fe-ions modified mesoporous Bi_2WO_6 nanosheets with high visible light photocatalytic activity, J. Colloid Interface 369 (2012) 373–380.

[23] F. Auzel, Upconversion processes in coupled ion systems, J. Lumin. 45 (1990) 341–345.

[24] Y.Y. Guo, D.Y. Wang, F. Wang, Effect of Li^+ ions doping on microstructure and upconversion luminescence of CeO_2:Er^{3+} translucent ceramics, Opt. Mater. 42 (2015) 390–393.

[25] Y.M. Ma, H.L. Liu, Z.Z. Han, L.B. Yang, J.H. Liu, Non-ultraviolet photocatalytic kinetics of $NaYF_4$:Yb, Tm@TiO_2/Ag Core@comby shell nanostructures, J. Mater. Chem. A 3 (2015) 14642–14650.

[26] S. Obregón, G. Colón, Heterostructured Er^{3+} doped $BiVO_4$ with exceptional photocatalytic performance by cooperative electronic and luminescence sensitization mechanism, Appl. Catal. B: Environ. 158–159 (2014) 242–249.

[27] H. Liu, M. Luo, J.C. Hu, β-Bi_2O_3 and Er^{3+} doped β-Bi_2O_3 single crystalline nanosheets with exposed reactive {001} facets and enhanced photocatalytic performance, Appl. Catal. B: Environ. 140–141 (2013) 141–150.

[28] Y.Y. Luo, G.Q. Tan, Effects of structure morphology, and up-conversion on Nd-doped $BiVO_4$ system with high photocatalytic activity, Ceram. Int. 41 (2015) 3259–3268.

[29] J. Reszczyńska, T. Grzyb, Z. Wei, M. Klein, E. Kowalska, B. Ohtani, A. Zaleska-Medynska, Photocatalytic activity and luminescence properties of RE^{3+}-TiO_2 nanocrystals prepared by sol-gel and hydrothermal methods, Appl. Catal. B: Environ. 181 (2016) 825–837.

[30] M. Pokhrel, G.A. Kumar, D.K. Sardar, Highly efficient NIR to NIR and VIS upconversion in Er^{3+} and Yb^{3+} doped in M_2O_2S (M = Gd, La Y), J. Mater. Chem. A 1 (2013) 11595–11606.

[31] J.S. Xu, T.J.K. Brenner, Z.P. Chen, D. Neher, M. Antonietti, M. Shalom, Different upconversion properties of β-$NaYF_4$:Yb^{3+}, Tm^{3+}/Er^{3+} in affecting the near-infrared-driven photocatalytic activity of high-reactive TiO_2, ACS Appl. Mater. Interfaces 6 (2014) 16481–16486.

[32] S.Y. Liu, Y.D. Wang, Catalytic photodegradation of Congo red in aqueous solution by $Ln(OH)_3$ (Ln = Nd, Sm Eu, Gd, Tb, and Dy) nanorods, Appl. Catal. A: Gen. 453 (2013) 45–53.

[33] J.L. Han, G.Q. Zhu, M. Hojamberdiev, J.H. Peng, P. Liu, Temperature effect on phase transition and morphological transformation of BiOI microspheres to Bi_5O_7I microstructures, Mater. Lett. 169 (2016) 122–125.

[34] S. Obregón, G. Colón, Improved O_2 evolution from a water splitting reaction over Er^{3+} and Y^{3+} co-doped tetragonal $BiVO_4$, Catal. Sci. Technol. 4 (2014) 2042–2050.

[35] S. Obregón, S.W. Lee, G. Colón, Exalted photocatalytic activity of tetragonal $BiVO_4$ by Er^{3+} doping through a luminescence cooperative mechanism, Dalton Trans. 43 (2014) 311–316.

[36] B. Chai, X. Wang, Enhanced visible light photocatalytic activity of BiOI/BiOCOOH composites synthesized via ion exchange strategy, RSC Adv. 5 (2015) 7589–7596.

[37] B.X. Wang, W.J. An, Novel Cu_2S quantum dots coupled flower-like BiOBr for efficient photocatalytic hydrogen production under visible light, RSC Adv. 5 (2015) 3224–3231.

[38] J. Luo, X.S. Zhou, L. Ma, X.Y. Xu, Enhanced visible-light-driven photocatalytic activity of WO_3/BiOI heterojunction photocatalysts, J. Mol. Catal. A: Chem. 410 (2015) 168–176.

[39] W. Liu, X. Zhao, A.G.L. Borthwick, Y.Q. Wang, J.R. Ni, Dual-enhanced photocatalytic activity of Fe-deposited titanate nanotubes used for simultaneous removal of As(III) and As(V), ACS Appl. Mater. Interfaces 7 (2015) 19726–19735.

[40] D.X. Hou, R. Goei, X.P. Wang, P.H. Wang, T.T. Lim, Preparation of carbon-sensitized and Fe-Er codoped TiO_2 with response surface methodology for bisphenol A photocatalytic degradation under visible-light irradiation, Appl. Catal. B: Environ. 126 (2012) 121–133.

[41] T. Xiong, X.A. Dong, H.W. Huang, W.L. Cen, Y.X. Zhang, F. Dong, Single precursor mediated-synthesis of Bi semimetal deposited N-Doped $(BiO)_2CO_3$ superstructures for highly promoted photocatalysis, ACS Sustain. Chem. Eng. 4 (2016) 2969–2979.

[42] J.S. Xu, T.J.K. Brenner, Z.P. Chen, D. Neher, M. Antonietti, Upconversion-agent induced improvement of g-C_3N_4 photocatalyst under visible light, ACS Appl. Mater. Interfaces 6 (2014) 16481–16486.

[43] V.D. Rodríguez, V.K. Tikhomirov, J.J. Velaízquez, M.V. Shestakov, V.V. Moshchalkov, Visible-to-UV/violet upconversion dynamics in Er^{3+}-doped oxyfluoride nanoscale glass ceramics, Adv. Opt. Mater. 1 (2013) 747–752.

[44] J.P. Perdew, M. Levy, Physical content of the exact Kohn-Sham orbital energies: band gaps and derivative discontinuities, Phys. Rev. Lett. 51 (1983) 1884–1887.

[45] L. Chen, S.F. Yin, S.L. Luo, R. Huang, Q. Zhang, T. Hong, $Bi_2O_2CO_3$/BiOI photocatalysts with heterojunctions highly efficient for visible-light treatment of dye-containing wastewater, Ind. Eng. Chem. Res. 51 (2012) 6760–6768.

[46] S.J. Liang, S.Y. Zhu, Y. Chen, W.M. Wu, X.C. Wang, Rapid template-free synthesis and photocatalytic performance of visible light activated $SnNb_2O_6$ nanosheets, J. Mater. Chem. 22 (2012) 2670–2678.

[47] F. Dong, T. Xiong, Y.J. Sun, H.W. Huang, Z.B. Wu, Synergistic integration of thermocatalysis and photocatalysis on black defective $(BiO)_2CO_3$ microspheres, J. Mater. Chem. A 3 (2015) 18466–18474.

[48] N. Kameta, M. Masuda, H. Minamikawa, Y. Mishima, I. Yamashita, T. Shimizu, Functionalizable organic nanochannels based on lipid nanotubes: encapsulation and nanofluidic behavior of biomacromolecules, Chem. Mater. 19 (2007) 3553–3560.

[49] K. Fu, J.Z. Huang, N.N. Yao, X.J. Xu, M.Z. Wei, Enhanced photocatalytic activity of TiO_2 nanorod arrays decorated with CdSe using an upconversion TiO_2:Yb^{3+}, Er^{3+} thin Film, Ind. Eng. Chem. Res. 54 (2015) 659–665.

[50] A.S. Weber, A.M. Grady, R.T. Koodali, Lanthanide modified semiconductor photocatalysts, Catal. Sci. Technol. 2 (2012) 683–693.